A simple efficient algorithm for molecular simulations of constant potential electrodes

Ranisha S. Sitlapersad ; Anthony R. Thornton ; Wouter K. den Otter ✉

Check for updates

View Online   Export Citation   CrossMark

The Journal of Chemical Physics

2024 Emerging Investigators Special Collection

Submit Today

A simple efficient algorithm for molecular simulations of constant potential electrodes

View Online   Export Citation   CrossMark

Ranisha S. Sitlapersad, [iD] Anthony R. Thornton, [iD] and Wouter K. den Otter[a) [iD]

AFFILIATIONS

Department of Fluid and Thermal Engineering and MESA+ Institute for Nanotechnology, University of Twente, Enschede, The Netherlands

a)Author to whom correspondence should be addressed: w.k.denotter@utwente.nl

ABSTRACT

Increasingly, society requires high power, high energy storage devices for applications ranging from electric vehicles to buffers on the electric grid. Supercapacitors are a promising contribution to meeting these demands, though there still remain unsolved practical problems. Molecular dynamics simulations can shed light on the relevant molecular level processes in electric double layer capacitors, but these simulations are computationally very demanding. Our focus here is on the algorithmic complexity of the constant potential method (CPM), which uses dedicated electrostatics solvers to maintain a fixed potential difference between two conducting electrodes. We show how any standard electrostatics solver—capable of calculating the energies and forces on all atoms—can be used to implement CPM with a minimum of coding. As an example, we compare our generalized implementation of CPM, based on invocations of the particle–particle–particle–mesh routine of the Large-scale Atomic/Molecular Massively Parallel Simulator, with a traditional implementation based on a dedicated re-implementation of Ewald summation. Both methods yield comparable results on four test systems, with the former achieving a substantial gain in speed and improved scalability. The step from dedicated electrostatic solvers to generic routines is made possible by noting that CPM's traditional narrow Gaussian point-spread of atomic charges on the electrodes effectively endows point-like atoms with chemical hardness, i.e., an intra-atomic energy quadratic in the charge.

I. INTRODUCTION

As the world moves away from fossil fuels toward renewable energies, there is an increased need for better high energy, high power storage devices. To meet this demand, several novel technologies have been proposed.[1] One viable technology is supercapacitors, as they have a higher power density and a longer life cycle than batteries. Unfortunately, their energy density is typically lower than that of batteries.[2,3] Using ionic liquids as electrolytes increases the potential window and thereby the energy density, but their poor flow behavior in the nanoscale pores of the electrodes adversely affects the power density.

Molecular Dynamics (MD) simulations are a powerful tool to study the microscopic processes that give rise to a supercapacitor's macroscopic performance.[4–11] A critical component in these simulations is the current conducting electrode, which equalizes the electrostatic potentials of all atoms in an electrode; these

potentials are due to long range electrostatic interactions with all other charged atoms in the system. Siepmann and Sprik[12] introduced a method for simulating constant potential atomistic electrodes by treating the charges of the electrode atoms as additional degrees of freedom in an extended Lagrangian; their electrode atoms are surrounded by narrow Gaussian charge distributions, whereas point charges are common practice in MD. Later, Reed et al.[13] revised the Constant Potential Method (CPM) by introducing an explicit expression for the charges on all electrode atoms, matching the most likely charges in the extended Lagrangian approach. Nakano and Sato[14] modeled the electrode atoms as point charges; they also endowed the electrode atoms with electronegativity and "chemical hardness," i.e., an internal energy related to the charges of the atoms. Interestingly, they find that the nett effect of the narrow Gaussian charge distributions is identical to simulating electrode atoms as point charges endowed with chemical hardness.[14] In alternative simulation models of

13 February 2024 08:58:50

electrodes, Holm and co-workers[15,16] introduced an Induced Charge Calculation (ICC*) algorithm that considers electrodes as media of infinitely large dielectric constants, with induced charges limited to the boundary surfaces. The charge redistribution within an electrode is more restricted in the Lorentz–Drude model,[17] where a light-weight negative charge representing the fluctuating electron cloud is tethered to a positively charged nucleus. The interested reader is referred to recent reviews on microscopic simulations of supercapacitors.[18–20]

The computationally most demanding part of CPM simulations is the calculation of long range electrostatic interactions by Ewald summation.[21–23] Several authors have presented MD simulation codes based on two-dimensional or three-dimensional (3D) dedicated Ewald summations of the long range electrostatic interactions,[12,13,24–26] where the 3D implementation requires a slab correction[13,27,28] or a careful set-up.[29] The computational complexity of 3D Ewald summation varies between $\mathcal{O}(N^2)$ and a theoretical optimum of $\mathcal{O}(N^{3/2})$, where N denotes the system size, i.e., the total number of atoms in electrodes and electrolytes combined.[22,23]

Alternatively, there are mesh-based electrostatic solvers, like the Particle–Particle–Particle–Mesh (PPPM or P³M) method by Hockney and Eastwood,[30] which has a lower theoretical complexity of $\mathcal{O}(N \log N)$.[22,23] This lower complexity is also realized by ICC*.[15,16] Implementations of these mesh-based methods are available in standard MD packages. Recently, Ahrens-Iwers et al.[31,32] published a PPPM-based constant potential routine ELECTRODE in the Large-scale Atomic/Molecular Massively Parallel Simulator (LAMMPS). As already briefly mentioned earlier, in traditional implementations of CPM, the atoms of the electrodes have narrow Gaussian charge distributions, while the atoms of the electrolyte are treated as point charges. Since molecular dynamics simulations conventionally treat all charged atoms as point charges, the available long range electrostatic routines are based on point charges. Hence, to apply such a routine in traditional CPM, it has to be adapted to include the non-point charge electrode atoms; dedicated Ewald summation routines have been used by a number of groups,[12,13,24–26,33] while the ELECTRODE routine[31,32] is based on a dedicated implementation of PPPM.

Our aim here is to propose a Generalized Constant Potential Method (GCPM) that generalizes CPM to work in combination with any off-the-shelf electrostatic solver. The direct use of existing efficient electrostatic routines not only makes GCPM faster than traditional Ewald-based CPM routines but also simplifies the code and makes it more flexible. This becomes possible by following Nakano and Sato[14] in treating the electrode atoms as point charges and using chemical hardness as an energetic penalty on the atomic charge fluctuations, as discussed in detail below. The fact that GCPM can be implemented without (re)coding dedicated electrostatic solvers means any existing or future solver will do, provided it is capable of solving the forces and energies on all atoms. As an illustration of GCPM, we have implemented the algorithm in LAMMPS,[34,35] as this allowed us to build on and compare with the conventional Ewald-based implementation of CPM for LAMMPS by Wang et al.[25] We illustrate with numerical examples, by repeatedly doubling the size of four typical systems, that switching from Ewald summation to PPPM yields a considerable speedup and reduces the computational complexity.

This paper is organized as follows: in Sec. II, we describe our approach and its physical motivation in more detail. An implementation in LAMMPS is discussed in Sec. III, along with the descriptions of four model systems. Simulations on these systems using GCPM and CPM are compared in Sec. IV, where we observe excellent agreement in numerical results and a significant difference in time complexity. Run times are also compared with the highly tuned ELECTRODE routine. We end with a summary of our observations in Sec. V.

II. THEORY

Molecular dynamics simulations of ions near electrodes crucially depend on the evaluation of the charges on the electrode atoms, which will be the main topic of this section. The time evolution and probability distribution of the capacitor are determined by its energy function, which will be derived first, followed by its macroscopic electronic properties. Consider a system of n ions with fixed charges q_i and variable positions r_i confined between two electrodes containing a total of N atoms with variable charges Q_j and fixed positions R_j. The charge distributions on the conducting electrodes evolve in response to the motion of the ions, by thermal fluctuations of the electron clouds, and by charge exchange with an external voltage source that maintains a constant potential difference $\Delta V = V_R - V_L$ between the potentials V_R and V_L on the right and left electrodes, respectively. For brevity of notation, the charges are collected in the column vectors q and Q, respectively, while the collective sets of coordinates are denoted by r and R, respectively. The potentials of the wall particles are then represented by the vector

$$\boldsymbol{\Psi} = V_R \boldsymbol{E}_R + V_L \boldsymbol{E}_L = \Delta V \boldsymbol{D} + V_* \boldsymbol{E}, \tag{1}$$

where the elements of vector $\boldsymbol{E}_R$ ($\boldsymbol{E}_L$) are +1 for atoms on the right (left) electrode and zero for atoms on the other electrode, with vector $\boldsymbol{D} = (\boldsymbol{E}_R - \boldsymbol{E}_L)/2$ that takes the form $\boldsymbol{D} = (\frac{1}{2}, \ldots, \frac{1}{2}, -\frac{1}{2}, \ldots, -\frac{1}{2})$ if the atoms in the right electrode precede those in the left electrode in these collection vectors, potential offset $V_* = (V_R + V_L)/2$ and vector $\boldsymbol{E} = \boldsymbol{E}_R + \boldsymbol{E}_L = (1, \ldots, 1)$. Assuming that the atomic charges obey Boltzmann statistics, the probability distribution function of the capacitor in equilibrium with a heat bath at absolute temperature T reads as[24]

$$P(\boldsymbol{r}, \boldsymbol{Q}; \Delta V, V_*) d\boldsymbol{r} d\boldsymbol{Q} = \frac{1}{Z} e^{-\beta(U_Q + U_{\neq Q} - \boldsymbol{Q} \cdot \boldsymbol{\Psi})} d\boldsymbol{r} d\boldsymbol{Q}, \tag{2}$$

where the configuration integral Z normalizes the distribution and $\beta = 1/(k_B T)$ with Boltzmann constant k_B; in the exponential, the energy has been split into internal potential energy related to the charges, U_Q, internal potential energy unrelated to the charges, $U_{\neq Q}$, and work associated with the external potential source, $\boldsymbol{Q} \cdot \boldsymbol{\Psi}$. The charge-related internal potential U_Q comprises two contributions, an inter-atomic Coulombic energy and an intra-atomic excitation energy, to be discussed next.

The total Coulombic electrostatic energy of all atoms in the system is quadratic in the charges,

$$U_e = \frac{1}{2} \begin{pmatrix} \boldsymbol{Q} \\ \boldsymbol{q} \end{pmatrix}^T \begin{pmatrix} \mathbf{A} & \mathbf{B} \\ \mathbf{B}^T & \mathbf{C} \end{pmatrix} \begin{pmatrix} \boldsymbol{Q} \\ \boldsymbol{q} \end{pmatrix}, \tag{3}$$

where the symmetric $N \times N$ matrix $\mathbf{A}$, the non-symmetric $N \times n$ matrix $\mathbf{B}$, and the symmetric $n \times n$ matrix $\mathbf{C}$ are functions of the atomic positions, and the superscript T denotes a transposition. The matrices take into account that the simulation box is periodically continued in all three Cartesian directions, endowing every atom with an infinite number of interaction partners. While these matrices are convenient for the current derivation, dedicated routines like Ewald summation and PPPM calculate the electrostatic energy and force per atom—treating all atoms as point charges—by more efficient routes that bypass the evaluation of these matrices. The main step in Ewald summation is to add and subtract Gaussian charge distributions of width α^{-1} to every point charge, thereby enabling splitting the energy and force calculations into real space and reciprocal space contributions that both rapidly converge; PPPM uses a different spreading function, along with a grid for the reciprocal space contributions.[21–23,30,36,37] The resulting energy expression is briefly discussed in the Appendix. Because an explicit evaluation of $\mathbf{A}$ is required to obtain the charges of all electrode atoms in CPM, an analytic expression for the matrix elements is provided in Eq. (A3). Besides these inter-atomic energies related to the charges, there are also intra-atomic contributions accounting for the energy associated with the gain or loss of charge by the electrode atoms through exchange with neighboring atoms.[14,33,38] We will approximate this energy with a quadratic Taylor expansion,

$$U_p = U_p^{(0)} + U_p^{(1)} + U_p^{(2)} = \sum_i \left(U_i^0 + \kappa_i Q_i + \frac{1}{2} K_i Q_i^2 \right), \quad (4)$$

where the constant energy resulting from the zeroth-order terms, $U_p^{(0)} = \sum_i U_i^0$, is of no consequence and will, therefore, be ignored henceforth. The coefficients κ_i and K_i originate in the quantum behavior of electrons in the metallic electrode and have recently been related to material properties in the Thomas–Fermi model.[33] In the chemical context of charge redistribution within a molecule, κ_i is known as the electronegativity and K_i as the hardness.[14,38,39] The current study uses electrodes of one atom type only, hence $\kappa_i = \kappa$ and $K_i = K$ for all i. The sum contribution of the first-order terms $U_p^{(1)} = \sum_i \kappa_i Q_i = \kappa \mathbf{E} \cdot \mathbf{Q}$ then makes the same impact on the Boltzmann distribution of Eq. (2) as a shift of V_* in the external energy $\mathbf{Q} \cdot \mathbf{\Psi}$; thus, $U_p^{(1)}$ can be absorbed in V_* and will be omitted henceforth. The sum of the remaining quadratic terms, $U_p^{(2)} = (K/2) \sum_i Q_i^2$, effectively acts as a "penalty," limiting the atomic charge fluctuations, provided K is positive, as will be assumed henceforth. This energy is conveniently combined with the electrostatic term, $U_Q = U_e + U_p$, to obtain a quadratic expression of the form of Eq. (3) with the modified matrix $\mathbf{A}_p = \mathbf{A} + K\mathbf{1}$. Simulations of electrodes combining hardness with CPM are hampered by a hardness surreptitiously introduced by the traditional implementation of CPM,[14,33] as will be discussed next.

In traditional CPM, the electrode atoms are not treated as point charges but as narrow Gaussian charge distributions of width η^{-1}, which is not to be confused with the Gaussian distributions of width α^{-1} used in Ewald summation to facilitate the calculation of the electrostatic energy of a collection of point charges. The internal potential energy related to the charges is then given by $U_Q = U_e^{\text{CPM}}$, with the full expression provided in the Appendix. As a result of the narrow Gaussian spreading, contributions to $\mathbf{A}$ of the form $\text{erfc}(\alpha R_{ij})/R_{ij}$ in regular Ewald summation, with erfc the

complementary error function and R_{ij} the distance between electrode atoms i and j, are supplemented in CPM's energy-charge matrix $\mathbf{A}_{\text{CPM}}$ by terms of the form $\text{erfc}(\eta R_{ij}/\sqrt{2})/R_{ij}$, as detailed in the Appendix. For the typical value $\eta = 1.979$ Å^{-1} in the literature,[13,25] the carbon–carbon bond length $R_{CC} = 1.42$ Å in graphene yields $\text{erfc}(\eta R_{CC}/\sqrt{2}) = 5 \times 10^{-3}$, while the typical value $\alpha = 0.18$ Å^{-1} gives a 145-fold larger $\text{erfc}(\alpha R_{CC}) = 0.72$. This ratio grows larger with increasing distance between the atoms, as does its counterpart for electrode–ion interactions, which already reaches 10^4 for a distance as small as 1.42 Å. Consequently, one may safely ignore the additional complementary error functions incurred in $\mathbf{A}_{\text{CPM}}$ by the narrow spreading of the wall charges, as will also be borne out by the simulation results presented below. Inspection of the CPM energy expression in the Appendix reveals that the narrow spread does also yield a non-negligible energy contribution, namely the underlined term of Eq. (A5),

$$4\pi\varepsilon_0 \left(U_e^{\text{CPM}} - U_e \right) = \frac{\eta}{\sqrt{2\pi}} \mathbf{Q} \cdot \mathbf{Q}, \quad (5)$$

with ε_0 the dielectric permittivity of a vacuum. Upon comparing this expression with Eq. (4), we conclude that η effectively acts as the hardness of the electrode atoms. By rewriting the penalty in the same form, $4\pi\varepsilon_0 U_p = (1/2)K'\mathbf{Q} \cdot \mathbf{Q}$, it follows that traditional CPM corresponds to

$$K' = \sqrt{\frac{2}{\pi}} \eta, \quad (6)$$

as was previously derived via an alternative route by Nakano and Sato.[14] The common value of $\eta = 1.979$ Å^{-1} then introduces a hardness $K' = 1.579$ Å^{-1}. We verified that under this particular condition, CPM and GCPM produce similar charges $\mathbf{Q}$ on the electrode atoms for atomic configurations satisfying the above typical minimum distances between the atoms. For this particular value of K', the energy penalty of endowing a neutral atom with a unit charge $\pm e$ amounts to ≈ 11.4 eV. This value is similar to the experimental ionization energies of an isolated atom of 9.2, 7.7, and 11.3 eV for gold, copper, and carbon, respectively;[40] the smallest energy to release an electron from a bulk material, i.e., the work function, has been measured as $W = 4.3–4.7$, $4.5–5.1$, and 4.4 eV for the two corresponding metals (with the ranges accounting for variations across crystal surfaces) and few-layer graphene, respectively.[41,42] While these numbers lend some credibility to the default values of η and K', it should be noted that the penalty is a simplified classical approximation of the quantum effects at modest charge fluctuations, while charge fluctuations of $\pm e$ are taking this model to its extreme.

Because the electron distribution evolves on a much shorter time scale than the atomic motions, one may assume that the former is continuously in equilibrium with the configurations sampled in an MD simulation, i.e., the Born–Oppenheimer approximation. The charges of the electrode atoms, $\mathbf{Q}_*$, are then obtained by minimizing the total charge-related energy in the Boltzmann distribution—due to Coulombic interactions in Eq. (3), the penalty in Eq. (4), and the external potential source—with respect to the electrode charges,[13,25,43]

$$\frac{\partial (U_Q - \mathbf{Q} \cdot \mathbf{\Psi})}{\partial \mathbf{Q}} \bigg|_{\mathbf{Q}_*} = \mathbf{A}_p \mathbf{Q}_* + \mathbf{B}q - \mathbf{\Psi} = \mathbf{0}, \quad (7)$$

with solution

$$Q_*(r; \Delta V, V_*) = \mathbf{A}_p^{-1}(\Psi - \mathbf{B}q). \tag{8}$$

Electrostatic solvers require the system to be charge neutral, which is not the case in early implementations of CPM based on the above-mentioned equation.[25] For a neutral electrolyte, $\sum_j q_j = 0$, overall neutrality implies that the combined electrodes must be neutral too. This is realized by selecting the potential V_* such that the electrodes' atomic charges add up to zero,

$$\sum_i Q_i^* \Big|_{V_*} = \mathbf{E} \cdot \mathbf{A}_p^{-1}(\Delta V \mathbf{D} + V_* \mathbf{E} - \mathbf{B}q) = 0, \tag{9}$$

yielding the potential offset

$$V_* = -\frac{\mathbf{E} \cdot \mathbf{A}_p^{-1}(\Delta V \mathbf{D} - \mathbf{B}q)}{\mathbf{E} \cdot \mathbf{A}_p^{-1}\mathbf{E}}. \tag{10}$$

Insertion of this result in Eq. (8) gives the charges of the electrode atoms as

$$Q_* = \mathbf{S}_p(\Delta V \mathbf{D} - \mathbf{B}q), \tag{11}$$

where the constant symmetric $N \times N$ matrix[43]

$$\mathbf{S}_p = \mathbf{A}_p^{-1}\left(1 - \mathbf{E}\frac{\mathbf{E} \cdot \mathbf{A}_p^{-1}}{\mathbf{E} \cdot \mathbf{A}_p^{-1}\mathbf{E}}\right), \tag{12}$$

has the projection property $\mathbf{S}_p\mathbf{E} = \mathbf{E} \cdot \mathbf{S}_p = 0$. Hence, Eq. (11) is equivalent to $Q_* = \mathbf{S}_p(\Psi - \mathbf{B}q)$, and the charges on the electrodes are independent of the potential offset V_*. Because the electrode charges are now enslaved to the ion coordinates, the probability density distribution sampled in the simulation reads as

$$P_*(r; \Delta V)dr = \frac{1}{Z_*}e^{-\beta(U_Q + U_{*Q} - Q_* \cdot \Psi)}dr, \tag{13}$$

where the configuration integral Z_* normalizes the distribution, the energy U_Q is evaluated using the charges $Q_*(r; \Delta V)$, and where the vanishing total charge on the electrodes implies $Q_* \cdot \Psi = \Delta V Q_* \cdot \mathbf{D}$.

Simulations sampling the distribution P_* require the charge-related forces on the electrolyte atoms, which are obtained for ion i by differentiating the charge-related potential energy in the exponent of Eq. (13) with respect to its position,

$$\begin{aligned}
f_i^Q &= -\frac{\partial(U_Q - Q_* \cdot \Psi)}{\partial r_i} \\
&= -\left(\frac{\partial U_Q}{\partial r_i}\right)_{Q_*} + \left(\frac{\partial Q_* \cdot \Psi}{\partial r_i}\right)_{Q_*} - \frac{\partial(U_Q - Q \cdot \Psi)}{\partial Q}\Big|_{Q_*} \cdot \frac{\partial Q_*}{\partial r_i},
\end{aligned} \tag{14}$$

where the first two derivatives of the last r.h.s. are evaluated at constant electrode atom charges Q_*, while the third term takes into account that these charges vary with the positions of the electrolyte atoms. Focusing now on these three terms, in the first term, with $U_Q = U_e + U_p$, the penalty does not depend on the position, and we are left with the usual electrostatic force, $f_i^e = -(\partial U_e/\partial r_i)_{Q_*}$, calculated

with the instantaneous electrode point charges Q_*. In the dot product of the third term, the first gradient equals zero, as this gradient was used to obtain the charges Q_* in Eq. (7). In the second term, upon inserting Eq. (1),

$$\left(\frac{\partial Q_* \cdot \Psi}{\partial r_i}\right)_{Q_*} = \left(\frac{\partial Q_* \cdot \Delta V \mathbf{D}}{\partial r_i}\right)_{Q_*} + \left(\frac{\partial Q_* \cdot V_* \mathbf{E}}{\partial r_i}\right)_{Q_*}, \tag{15}$$

we find that the first term on the r.h.s. vanishes because both the potential difference ΔV and the vector $\mathbf{D}$ are independent of the ion position, while the second term on the r.h.s. vanishes identically for charge-neutral electrodes, $Q_* \cdot \mathbf{E} = 0$. Under this latter condition, therefore, once the electrode charges Q_* are known, the forces on the ions are readily calculated using standard electrostatic routines: $f_i^Q = f_i^e$.

From a macroscopic perspective, one is interested in the total charges on the electrodes and the capacitance relating these charges to the potential difference. The time average charge on the right electrode in a thermostatted simulation will match its canonical ensemble average,

$$\langle Q_R\rangle_{\text{MD}} = \langle \mathbf{E}_R \cdot Q_*\rangle_* = \langle \mathbf{D} \cdot Q_*\rangle_*, \tag{16}$$

where the pointed brackets denote averages, with the subscript MD and asterisk referring to the simulations and Boltzmann distribution P_*, respectively, and where in the last step the charge on the right electrode is calculated as an average over both electrodes by using that $Q_L = -Q_R$ and hence $Q_R = (Q_R - Q_L)/2$. A straightforward, though a bit laborious, differentiation[24,43,44] using

$$\frac{\partial Q_*}{\partial \Delta V} = \mathbf{S}_p\mathbf{D}, \tag{17}$$

and

$$\frac{\partial U_Q}{\partial \Delta V} = \mathbf{D} \cdot \mathbf{S}_p^T(\mathbf{A}_p Q_* + \mathbf{B}q) = \Delta V \mathbf{D} \cdot \mathbf{S}_p\mathbf{D}, \tag{18}$$

then yields the average charge

$$\langle Q_R\rangle_* = k_B T \frac{\partial \ln Z_*}{\partial \Delta V} + \Delta V \mathbf{D} \cdot \mathbf{S}_p\mathbf{D}, \tag{19}$$

and the differential capacitance

$$C_* = \frac{\partial \langle Q_R\rangle_*}{\partial \Delta V} = \beta\big(\langle Q_R^2\rangle_* - \langle Q_R\rangle_*^2\big) + \mathbf{D} \cdot \mathbf{S}_p\mathbf{D}. \tag{20}$$

The first terms on the r.h.s. of the last two equations are identical, except for the asterisks, to the average charge and capacitance derived from Eq. (2) for electrode charges that are not enslaved to the ion positions; the unexpected second terms appearing on the r.h.s. are consequences of the particular ensemble being sampled. Since these are the only terms that remain when the ions are removed, it follows that they represent direct inter-electrode contributions to the electrode charge and capacitance. Identical expressions were derived by Scalfi et al.[43] using the projected vector $\mathbf{D}_{\text{Scalfi}} = \mathbf{D} - \mathbf{E}(\mathbf{D} \cdot \mathbf{E})/(\mathbf{E} \cdot \mathbf{E})$, which reduces to $\mathbf{D}_{\text{Scalfi}} = (\alpha_R, \ldots, \alpha_R, \alpha_L, \ldots, \alpha_L)$ with $\alpha_R = N_L/(N_R + N_L)$ and $\alpha_L = -N_R/(N_R + N_L)$ if the N_R atoms of the right electrode precede the N_L atoms of the left electrode; one readily verifies that replacing the $\mathbf{D}$-s in the above second terms with their

projections is of no consequence due to the projection properties of $\mathbf{S}_p$. Extending the simulated ensemble average in post-processing by superimposing the previously eliminated fluctuations of $\boldsymbol{Q}$ around $\boldsymbol{Q}_*$ will not affect the mean electrode charge since these fluctuations are symmetrically distributed around $\boldsymbol{Q}_*$ for a quadratic U_Q. Hence, following the first step in Eq. (20), these rapidly fluctuating charges will not affect the differential capacitance either.[43]

III. METHODS AND SYSTEMS

A. Methods

We implemented GCPM in LAMMPS[45] because its implementation of a traditional Ewald-based CPM by Wang *et al.*,[25] available on GitHub,[46] offers a convenient testing ground. We had to make only minimal modifications to LAMMPS for our purposes, which are available on GitHub.[47]

In Sec. II, we observed that the forces on the electrolyte atoms can be calculated using any electrostatics routine once the charges $\boldsymbol{Q}_*$ on the electrodes are known, see Eq. (14). To obtain these charges [see Eqs. (11) and (12)] one must evaluate the matrices $\mathbf{A}_p$ and $\mathbf{S}_p$ and the vector $\mathbf{B}\boldsymbol{q}$. We opt here for the PPPM method rather than the Ewald summation traditionally used in CPM because the former is of lower complexity: whereas Ewald summation scales as $\mathcal{O}(N_{\text{tot}}^{3/2})$ at best, PPPM realizes $\mathcal{O}(N_{\text{tot}} \ln N_{\text{tot}})$, where N_{tot} is the total number of atoms in the system. The calculation of $\mathbf{A}_p$, and consequently that of $\mathbf{S}_p$, is much more demanding than that of $\mathbf{B}\boldsymbol{q}$; one, therefore, commonly freezes the electrode atoms in CPM simulations to avoid repeated evaluations of these matrices. One may choose to occasionally displace the walls as rigid units or pistons to introduce pressure control, as in the MetalWalls routine,[26] at the expense of recalculating $\mathbf{A}_p$ and $\mathbf{S}_p$ and the vector $\boldsymbol{V}_0'$ to be introduced below; for frequent updates of $\mathbf{A}_p$, the solution of Eq. (11) by (preconditioned) conjugate gradient minimization[26] becomes preferable over the current solution by matrix multiplication. The configuration-dependent vector $\mathbf{B}\boldsymbol{q}$ requires recalculation in every step and thereby dominates the time complexity of (G)CPM. We, therefore, first focus on the calculation of this vector, which physically represents the electrostatic potentials on the electrode atoms due to the electrolyte. Suppose one replaces the charges on the electrode atoms by small non-zero test charges on all atoms, $\boldsymbol{Q}'$, while retaining neutrality, $\boldsymbol{E} \cdot \boldsymbol{Q}' = 0$; for instance, we used $\boldsymbol{Q}' = Q'\boldsymbol{D}$ with $Q' = 2 \times 10^{-3}e$ for systems with two electrodes of $N/2$ atoms each. We next invoke an electrostatics solver to determine the resulting electrostatic energies, $\boldsymbol{U}'$, of all electrode atoms. Dividing each of these energies by half their corresponding atomic charge yields the potential of atom i as $\left(\boldsymbol{V}_q'\right)_i = 2U_i'/Q_i'$, whereas Eq. (3) gives

$$\boldsymbol{V}_q' = \mathbf{A}\boldsymbol{Q}' + \mathbf{B}\boldsymbol{q}. \tag{21}$$

Note that the vector $\boldsymbol{V}_0' = \mathbf{A}\boldsymbol{Q}'$, representing the potentials on the electrodes induced by the electrodes, remains constant during the simulation if the atomic positions $\boldsymbol{R}$ and the charges $\boldsymbol{Q}'$ remain constant; $\boldsymbol{V}_0'$ is readily evaluated at the start of the simulation by turning off the electrolyte charges, $\boldsymbol{q} = \mathbf{0}$. The desired potentials on the electrodes due to the electrolyte are then obtained as $\mathbf{B}\boldsymbol{q} = \left(\boldsymbol{V}_q' - \boldsymbol{V}_0'\right)$. In summary, GCPM requires two invocations of an electrostatic solver in every time step: once with the charges $\boldsymbol{Q}'$ to determine the poten-

tials $\mathbf{B}\boldsymbol{q}$ and thence the electrode charges $\boldsymbol{Q}_*$, and once with these charges $\boldsymbol{Q}_*$ to evaluate the forces on the electrolyte that propagate the system. Both invocations are expected to scale to $\mathcal{O}(N_{\text{tot}} \ln N_{\text{tot}})$ when using PPPM as the electrostatic solver.

The matrix $\mathbf{A}$ was calculated using the CPM routines developed by Wang *et al.*[25] for LAMMPS, as available on GitHub.[46] Care was taken to remove all calculations relating to the point-spread of the electrode atoms, thus obtaining the matrix $\mathbf{A}$ for a collection of point charges. In practice, this routine becomes very slow for large systems. We, therefore, developed an alternative approach that takes advantage of a lower complexity electrostatic solver. The diagonal elements are still calculated using regular Ewald summation, see Eq. (A3), by combining a single summation in reciprocal space—identical for all diagonal elements—with a trivial atom-specific term. Suppose we introduce test charges Q' and $-Q'$ on electrode atoms i and j, while all other atoms of the electrode and electrolyte are neutral. Invoking an electrostatics solver gives the Coulombic energy of atom i as

$$U_i' = \frac{1}{2}Q_i(A_{ii}Q_i + A_{ij}Q_j), \tag{22}$$

which is readily solved for A_{ij}. The energy of atom j does not provide additional information, while all other atoms are at non-zero potential but zero energy. Filling in the entire matrix $\mathbf{A}$ then requires $N(N-1)/2$ calls of the electrostatic solver. Suppose now that we introduce a charge vector, placing a charge $(N-1)Q'$ on the kth electrode atom and opposite charges $-Q'$ on all remaining $N-1$ electrode atoms,

$$\left(\boldsymbol{Q}_k'\right)_i = Q'(N\delta_{ki} - 1), \tag{23}$$

where δ_{ki} denotes the Kronecker delta. With the charges of the electrolyte turned off, $\boldsymbol{q} = \mathbf{0}$, the resulting potentials on all electrode atoms, $\boldsymbol{V}_k' = \mathbf{A}\boldsymbol{Q}_k'$, are readily calculated from the energies $\boldsymbol{U}_k'$ returned by the electrostatic solver. The difference between two charge vectors describes a state with only two charged atoms,

$$\left(\boldsymbol{Q}_k' - \boldsymbol{Q}_l'\right)_i = NQ'(\delta_{ki} - \delta_{li}), \tag{24}$$

and potentials

$$\left(\boldsymbol{V}_k' - \boldsymbol{V}_l'\right)_j = NQ'(A_{kj} - A_{lj}). \tag{25}$$

Hence, for $j = l$,

$$A_{kl} = \frac{1}{NQ'}\left(\boldsymbol{V}_k' - \boldsymbol{V}_l'\right)_l + A_{ll}. \tag{26}$$

It follows that once the diagonal elements are known, all off-diagonal elements can be calculated by sequentially passing the N charge distribution vectors $\boldsymbol{Q}_k'$ through the electrostatic solver. The evaluation of $\mathbf{A}$ is then expected to scale to $\mathcal{O}(N^2 \ln N)$ when using PPPM as the electrostatic solver. With these modifications, the calculation of $\mathbf{A}_p$ is of lower complexity than its subsequent conversion into $\mathbf{S}_p$ by Eq. (12), and the calculation of $\mathbf{B}\boldsymbol{q}$ is of lower complexity than its subsequent conversion into $\boldsymbol{Q}_*$ by Eq. (11). These conversions will dominate the scaling behavior for large systems, much larger than the practical examples discussed here, in which case Eq. (11) is more efficiently solved by (preconditioned) conjugate gradient minimization.[26]

B. Systems

We compare the results and performances of CPM and GCPM for four model systems (see Fig. 1). The first system is identical to the reference system in Ref. 48. It has graphene-like electrodes, separated by H = 4 nm, and a potential difference ΔV = 0.2 V. Each electrode has an area of A = 25.15 nm^2 and consists of one layer of 960 frozen particles with inter-particle bond lengths of 0.142 nm. The simulation box is periodically repeated in space, with the box length perpendicular to the electrodes extended to $3H$. The system contains 51 ion pairs, corresponding to a reservoir concentration of 1M (see Ref. 48), with ionic charges $q_i = \pm e$; the total number of particles amounts to N_{tot} = 2022. Coulombic interactions are calculated using PPPM, using a cut-off distance of 1.2 nm in real space (`pair style coul/long`) and a relative accuracy of 10^{-6} in the long range forces. In the absence of an explicit solvent, the impact of an aqueous solvent on the electrostatic interactions is mimicked by introducing a relative permittivity of ε_r = 78. This scaling of the Coulombic energies and forces is appropriate for ions separated by many water molecules, while at shorter distances, the interaction will depend on the actual configuration of the water molecules; the variable charges on the electrode atoms very effectively screen Coulombic interactions within the electrodes. While ε_r can be set in LAMMPS, the current implementation of CPM[25] does not utilize this value and always assumes vacuum permittivity. Hence, we account for the relative permittivity by dividing all ion charges by $\sqrt{\varepsilon_r}$ and multiplying the potential difference by $\sqrt{\varepsilon_r}$; the simulation results reported below are corrected for this

expedient. Non-electrostatic interactions between all particle pairs are described by the Weeks–Chandler–Andersen (WCA) potential,

$$u(r_{ij}) = \begin{cases} 4\varepsilon\left[\left(\dfrac{\sigma}{r_{ij}}\right)^{12} - \left(\dfrac{\sigma}{r_{ij}}\right)^{6}\right] + \varepsilon, & r_{ij} < 2^{1/6}\sigma, \\ 0, & r_{ij} > 2^{1/6}\sigma, \end{cases} \quad (27)$$

with diameter σ = 5 Å and strength $\varepsilon = k_B T$ matching the thermal energy at the prevalent temperature T = 298 K. The motions of the ions are simulated using the Langevin equation,

$$m\ddot{\mathbf{r}}_i = -\xi\dot{\mathbf{r}}_i + \mathbf{f}_i + \mathbf{f}_i^R(t), \quad (28)$$

with ions weighing in at m = 50 atomic mass units (a.m.u.), the dots denoting time derivatives, Stokesian drag coefficient ξ = 2.26 a.m.u./fs for spherical particles of diameter σ in water, conservative force $\mathbf{f}_i$, and zero-mean Markovian random forces $\mathbf{f}_i^R$, whose variance is related to the drag coefficient and the temperature by the fluctuation-dissipation theorem. The equations of motion are integrated using the velocity-Verlet scheme with a time step Δt = 5 fs.

The second system is similar to the first system [see Fig. 1(b)], so we only describe the differences. Both electrodes consist of three FCC (111) layers of 90 particles each, with a nearest-neighbor distance of 1.12σ, covering an area A = 24.55 nm^2. The distance between the two innermost electrode layers is again H = 4 nm, and
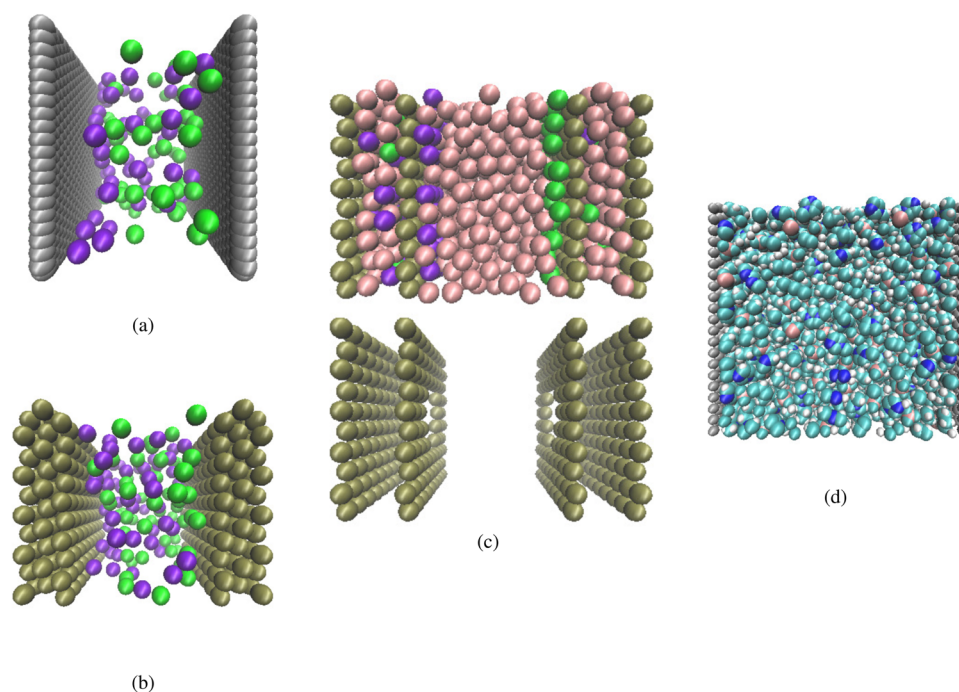
FIG. 1. Snapshots of the four systems used to compare CPM with GCPM: (a) ions (green and purple) in implicit solvent between graphene-like electrodes (gray), (b) ions in implicit solvent between FCC electrodes (yellow), (c) ions in explicit solvent (pink) between porous electrodes, shown here with and without the electrolyte, and (d) the ionic liquid [BMIM$^+$][BF$_4^-$] (colors) between copper electrodes (gray).

the box height equals three times the distance between the two outermost electrode layers. The system contains 59 ion pairs, corresponding to a reservoir concentration of ≈1M; consequently, these first two systems have approximately matching ion concentrations in the ion-depleted central region between the two double layers. The total number of particles in this system is 658.

The third system uses model porous electrodes and explicit solvent [see Fig. 1(c)] to reproduce the enlarged surface area and flow bottlenecks of supercapacitors. Both electrodes consist of two FCC (111) layers separated by 1.5 nm, with the two outermost layers identical to the layers in the previous system. The distance between the two innermost electrode layers is again 4 nm, and the box height equals three times the distance between the two outermost electrode layers. The applied potential difference between the two electrodes is 2 V. The two innermost layers contain circular holes of about 2 nm in diameter, created by removing 12 atoms from each layer. The flow restrictions due to these small pores reduce the (dis)charging rate of this supercapacitor. Since the interactions of the ions with solvent molecules will further impede the flow in real systems, the 94 ion pairs are supplemented with 752 neutral solvent particles, all endowed with identical WCA interactions, making a total of 1276 particles. The explicit solvent generates the Brownian motion of its solutes; hence, the evolution is modeled by regular MD, using velocity Verlet with a time step of 5 fs and employing a Nosé–Hoover thermostat with a time constant of 100 fs. Neutral solvent particles do not shield the electrostatic interactions between the ions; hence, the relative permittivity of $\varepsilon_r = 78$ is maintained to prevent the ions from crystallizing. A related system with both electrodes modeled as closely spaced fixed stacks of six graphene layers, with all but the outermost layer containing a randomly located 1 nm-radius pore, was studied by Mendez-Morales et al.[8]

The fourth system, the room temperature ionic liquid 1-n-butyl-3-methylimidazolium tetrafluoroborate $[BMIM^+][BF_4^-]$ between copper electrodes at $\Delta V = 0$ V, see Fig. 1(d), is also simulated by regular MD. The system contains 512 ion pairs, modeled using a reparametrization of the CL&P force field[49,50] by Mondal and Balasubramanian.[51] All bonds involving H atoms are constrained using the SHAKE algorithm.[52] Lennard-Jones parameters for the copper atoms, $\varepsilon_{Cu} = 0.52$ eV and $\sigma_{Cu} = 0.23$ nm, are copied from Filippova et al.[53] Both electrodes, separated by 5.73 nm, consist of one FCC (111) layer containing 504 atoms with a nearest-neighbor distance of $1.11\sigma_{Cu}$, covering an area of 28.52 nm². The total number of atoms amounts to 16 368. Lennard-Jones interactions are cut-off at 1.2 nm. The equations of motion are integrated using velocity Verlet with a time step of 1 fs, maintaining a temperature of 300 K by a Nosé–Hoover thermostat with a time constant of 1 ps.

Initial configurations for the first two systems were made by placing the ions on a lattice, while for the third system, the electrolyte particles were placed in random positions, followed by energy minimization with neutral walls, $\mathbf{Q} = \mathbf{0}$. These systems were thoroughly equilibrated for 20 ns, followed by production runs of 180 ns to determine the ensemble averages presented in Sec. IV. The fourth system was generated at random using the bulk fluid density, followed by energy minimization and 5 ns of equilibration; the subsequent production run covered 10 ns. Simulations with traditional Ewald-based CPM used the typical point spread parameter $\eta = 1.979$ Å⁻¹, while for the hardness parameter in

GCPM we evaluated the impacts of turning the hardness off, $K' = 0$, setting it equal to traditional CPM, $K' = \sqrt{2/\pi}\,\eta = 1.579$ Å⁻¹, and suppressing charge fluctuations more strongly, $K' = 10$ Å⁻¹. In both potentiostat approaches, the charges of the electrode atoms were updated at every step. Run times t_{run} of simulations using CPM, GCPM, and ELECTRODE for identical parameter settings were measured for a default serial compilation of LAMMPS on an Intel® Core™ i7-7700 at 3.60 GHz under Ubuntu 16.04.07 LTS. Identical starting configurations were run for $N_{step} = 10$, 100, and 1000 steps to establish the run time per step t_{step} by fitting $t_{run} = N_{step} t_{step} + t_0$, with t_0 accounting for the initialization and closure of the run. This procedure was repeated with systems containing multiple copies of the original unit cell by repeated doubling the system size while alternating between doubling along the two in-plane directions. The order of time complexity is obtained by fitting scaling laws,

$$t_{step} = aN_{tot}^b, \tag{29a}$$

$$t_{step} = c(N_{tot} \ln N_{tot})^d, \tag{29b}$$

with pre-factors a and c, powers b and d, and the total number of particles N_{tot}.

IV. RESULTS AND DISCUSSION

In this section, we present simulation results for four distinct systems. We compare charge distributions obtained with CPM and GCPM to verify whether both methods are in agreement. Run times are compared between CPM, GCPM, and ELECTRODE to establish the time complexities of the three methods.

A. Aqueous electrolyte between graphene-like electrodes

The density profiles of the ions of an aqueous electrolyte between two graphene-like electrodes, as obtained with GCPM using $K' = 1.579$ Å⁻¹ and a potential difference of 0.2 V, are presented in Fig. 2. With two identical electrodes and ions differing only in the sign of their charge, the distribution of anions relative to the anode will be identical to the distribution of cations relative to the cathode; this symmetry is highlighted in the main figure. The inset shows the difference between these density profiles and their counterparts obtained by CPM using $\eta = 1.979$ Å⁻¹, as studied earlier in Ref. 48. To quantify the observed good agreement, both production runs are divided into ten blocks to collect ten measurements of the ion concentrations for every bin along the z-direction. For every bin and both ion types, a pair-sampled t-test (ttest in MATLAB[54]) is used to test the null hypothesis that the pairwise difference between two sets of ten densities has a mean equal to zero. For the anions, the null hypothesis was rejected at the 5% significance level for only 5.2% of the bins (16 out of 307 non-empty bins); for the cations, the percentage rejected was even lower at 2.3% (7 out of 307 non-empty bins).

Like the ion distributions, the charge densities on the electrodes also show a very good agreement between CPM and GCPM at K' = 1.579 Å⁻¹, see Table I. The difference between the two charge densities amounts to about 0.002e/nm², or 0.3% of the average,
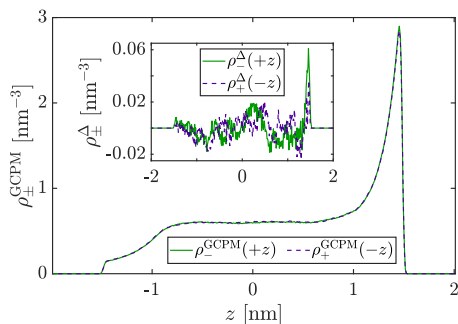
FIG. 2. Density profile of the anions $\rho_-(+z)$ and mirrored density profile of the cations $\rho_+(-z)$, for ions differing only in the signs of their charges, between two identical graphene-like electrodes at $\Delta V = 0.2$ V, see Fig. 1(a). The main plot shows simulation results obtained with GCPM, using $K = 1.579$ Å^{-1}. The differences between these density profiles and their counterparts obtained with CPM, $\rho_\pm^\Delta = \rho_\pm^{GCPM} - \rho_\pm^{CPM}$, are shown in the inset.

and is far lower than the standard deviation in the charge density of $\approx 0.045\,e/\mathrm{nm}^2$. The ionic contributions to the capacitances [see Eq. (20)] are also in good agreement. At about 6%, the difference is larger than that between the averages, in line with the common observation that an average requires less sampling to converge to the proper ensemble averaged value than a variance. The empty capacitances in CPM and GCPM are nearly identical, suggesting that the matrices $\mathbf{A}_p$ and $\mathbf{S}_p$ in GCPM are very similar to their counterparts

$\mathbf{A}_{CPM}$ and $\mathbf{S}_{CPM}$ in CPM. Based on the above-mentioned observations, we conclude that the two constant potential algorithms are sampling the same ensemble for $\eta \gtrsim 2$ Å^{-1} and $K' = \sqrt{2/\pi}\,\eta$.

Varying the strength of the penalty in GCPM, either by eliminating it completely or by a sixfold increase relative to the value used earlier, has a modest impact on the simulation results. Table I and Fig. 3 show that increasing the penalty to 10 Å^{-1} reduces the absolute charges on the electrodes and thereby makes them attract less co-ions and repel less counter-ions. The opposite effects are observed when the penalty is decreased, with the small deviations between the reference system and the $K' = 0$ system suggesting a modest impact of the penalty at the reference value of K'.

B. Aqueous electrolyte between FCC electrodes

The density profiles of the aqueous electrolyte between two FCC electrodes, as obtained with GCPM using $K' = 1.579$ Å^{-1}, and their differences with their counterparts calculated with CPM using $\eta = 1.979$ Å^{-1}, are presented in Fig. 4. The agreement between both sets of results is again excellent; the null hypothesis is rejected for anions in only 1.8% of bins (6 out of 330 non-empty bins) and for cations in 3.6% of bins (12 out of 329 non-empty bins). In Table I, it can be seen that the average charge densities on the electrodes differ by 0.003 e/nm^2, or 0.5%, well below the standard deviation of about 0.043 e/nm^2. The ionic contributions to the capacitances also agree well, differing by some 7%, while the empty capacitances are almost identical.

TABLE I. Average electrode charge $\langle \bar{Q} \rangle$, electrolyte contribution to the differential capacitance $C_{ions} = \beta\big(\langle \bar{Q}^2 \rangle - \langle \bar{Q} \rangle^2\big)$, and the empty capacitor contribution $C_{empty} = \boldsymbol{D} \cdot \boldsymbol{SD}$ for three systems under various conditions. All results are normalized per unit area parallel to the electrode, A. The simulations with GCPM, for three strengths of the penalty K', sample neutral configurations with electrode charges $\bar{Q} = Q_R = -Q_L$; C_{empty} is calculated using the matrix $\mathbf{S}_p$ defined in Eq. (12). Simulations with CPM, employing the usual narrow charge spreading η, sample non-neutral configurations with average electrode charge $\bar{Q} = (Q_R - Q_L)/2$; C_{empty} is calculated using the matrix $\mathbf{S}_{CPM}$ as obtained by Eq. (12) upon replacing $\mathbf{A}_p$ with $\mathbf{A}_{CPM}$. Note the good agreement between CPM and GCPM at $K' = \sqrt{2/\pi}\,\eta = 1.579$ Å^{-1} for the graphene and FCC systems; the modest agreement for the capacitance of the porous system is due to this system's slow sampling of phase space.

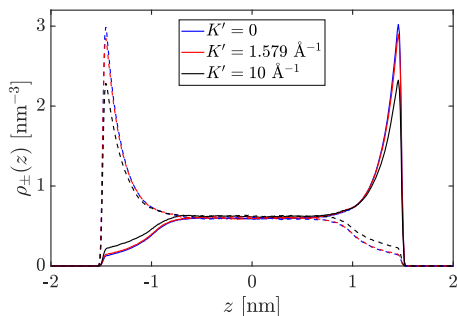| System	Method	η or K' $\left[\frac{1}{\text{Å}}\right]$	$\frac{\langle \bar{Q} \rangle}{A}$ $\left[\frac{e}{\text{nm}^2}\right]$	$\frac{C_{ions}}{A}$ $\left[\frac{e}{\text{V·nm}^2}\right]$	$\frac{C_{empty}}{A}$ $\left[\frac{e}{\text{V·nm}^2}\right]$
Graphene $\Delta V = 0.2$ V	CPM	1.979	0.640	2.02	1.09
	GCPM	0	0.669	2.13	1.10
		1.579	0.642	1.90	1.09
		10	0.508	1.52	1.00
FCC $\Delta V = 0.2$ V	CPM	1.979	0.577	1.84	1.01
	GCPM	0	0.520	1.48	0.97
		1.579	0.574	1.71	1.01
		10	0.292	0.70	0.75
Porous $\Delta V = 2$ V	CPM	1.979	5.555	0.39	0.97
	GCPM	0	6.165	1.63	1.18
		1.579	5.566	0.07	0.97
		10	3.315	0.87	0.63

FIG. 3. Density distributions of anions (solid lines) and cations (dashed lines) in an aqueous electrolyte between two graphene electrodes at $\Delta V = 0.2$ V. Varying the strength K' (colors) of the penalty function in GCPM has a minor effect on the ion distributions.
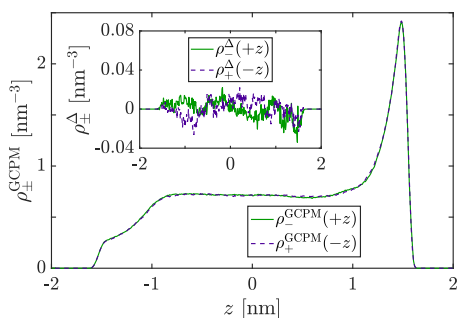

FIG. 4. Density profile of the anions $\rho_-(+z)$ and mirrored density profile of the cations $\rho_+(-z)$, for ions differing only in the signs of their charges, between two identical FCC electrodes at $\Delta V = 0.2$ V, see Fig. 1(b). The main plot shows simulation results obtained with GCPM, using $K = 1.579$ Å^{-1}. The differences between these density profiles and their counterparts obtained with CPM, $\rho_\pm^\Delta = \rho_\pm^{\mathrm{GCPM}} - \rho_\pm^{\mathrm{CPM}}$, are shown in the inset.

The ionic and charge distributions reveal an interesting dependence on the strength of the penalty function in GCPM. Decreasing the strength K' from the default value to zero hardly affects the counter-ion distributions at the electrodes, while more co-ions are attracted and a local concentration maximum appears adjacent to
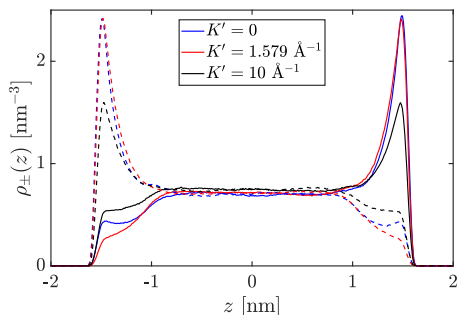

FIG. 5. Impact of the penalty parameter K' in GCPM on the density profiles of cations (dashed lines) and anions (solid lines) for an ionic solution between FCC electrodes.

the electrode (see Fig. 5). Table I shows, contrary to expectation, that releasing the penalty reduces the charge density on the electrodes by about 10% and decreases the capacitance by a similar fraction. A possible origin of these decreases may be found in the charge distribution within the electrode: Table II shows that for $K' = 0$, the charges on the three atomic layers per electrode are alternatingly positive and negative, with the largest absolute charge not on the layer facing the electrolyte but on the second layer, while the third layer also carries more charge than the first layer. Although some studies report alternating signs of the charges on consecutive layers, these differ from the non-monotonous decay of the absolute charge seen here for $K' = 0$. For example, in Refs. 55 and 56, the absolute charges per layer decrease monotonically with the distance from the electrode surface, with the charge per layer resembling a damped oscillation. In Ref. 25, the charge only alternates from the first layer to the second; the charges on the second and third layers are about -0.1 and -0.01 times the charge on the first electrode, respectively. For K' equal to or larger than the default value, as well as for CPM with the default value of η, the charge distribution decreases approximately exponentially with the depth below the electrolyte–electrode

TABLE II. Average surface charges and their standard deviations for the six atom layers of the FCC electrodes and the four atom layers of the porous electrodes [see Figs. 1(b) and 1(c)] as obtained using CPM and GCPM. The area is the same for all layers, $A = 24.55$ nm^2. The letters L and R in the names of the layers refer to the left and right electrodes, respectively, with the ordinal numbers increasing in the outward direction.

Method	η or K' [1/ Å]	Layer	$\langle \bar{Q}_{\mathrm{layer}} \rangle / A$ [e/nm^2] FCC	Porous
CPM	1.979	L3	-0.030 ± 0.003	
		L2	-0.104 ± 0.008	-2.27 ± 0.04
		L1	-0.444 ± 0.034	-3.29 ± 0.04
		R1	$+0.444 \pm 0.034$	$+3.28 \pm 0.04$
		R2	$+0.104 \pm 0.008$	$+2.27 \pm 0.04$
		R3	$+0.029 \pm 0.003$	
GCPM	0	L3	$+1.507 \pm 0.114$	
		L2	-2.726 ± 0.207	-0.63 ± 0.07
		L1	$+0.699 \pm 0.053$	-5.53 ± 0.07
		R1	-0.695 ± 0.053	$+5.56 \pm 0.07$
		R2	$+2.716 \pm 0.206$	$+0.60 \pm 0.07$
		R3	-1.501 ± 0.114	
	1.579	L3	-0.029 ± 0.002	
		L2	-0.103 ± 0.008	-2.28 ± 0.04
		L1	-0.442 ± 0.033	-3.29 ± 0.04
		R1	$+0.442 \pm 0.033$	$+3.29 \pm 0.03$
		R2	$+0.103 \pm 0.008$	$+2.28 \pm 0.04$
		R3	$+0.029 \pm 0.002$	
	10	L3	-0.074 ± 0.007	
		L2	-0.090 ± 0.008	-1.69 ± 0.02
		L1	-0.128 ± 0.012	-1.62 ± 0.02
		R1	$+0.128 \pm 0.012$	$+1.62 \pm 0.02$
		R2	$+0.090 \pm 0.008$	$+1.69 \pm 0.02$
		R3	$+0.074 \pm 0.007$	

interface; the decay length is 3.4 Å for the default K' and increases to 17 Å for $K' = 10$ Å^{-1}. This strengthening of the penalty reduces the build-up of charges on the first layer and thereby reduces the screening of subsequent layers from the electrolyte, resulting in an increased decay length. At the same time, the reduced charging leads to a lower overall charge of the electrode, a reduction in the counter-ion concentration adjacent to the electrode, and an increase in the co-ion concentration.

C. Ions in explicit solvent between porous electrodes

Figure 6 shows the density profiles for an electrolyte consisting of ions and neutral particles between model porous electrodes [see Fig. 1(c)], as obtained with GCPM. All three values of K' yield minima and maxima in the density at the same positions, the main differences being limited to the relative heights at these positions and the charges on the electrode layers. In the interior of both electrodes, for 2.0 nm $\leq |z| \leq 3.5$ nm, two layers are formed by counter-ions and neutral solvent particles. For $K' = 0$, these ions favor the inner wall, which, following Table II, carries a much larger charge than the outer wall, whereas for larger K', the ions shift to the outer wall, and
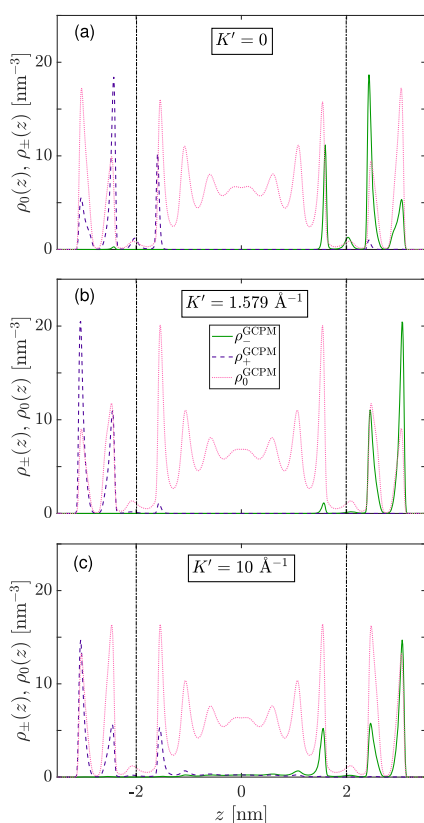
the charge difference between both walls decreases to nearly vanish for $K' = 10$ Å^{-1}. The liquid in the wider gap between the two electrodes, -2.0 nm $\leq z \leq 2.0$ nm, shows the typical decaying oscillations of a high density fluid under confinement. The ions in this gap are concentrated against the electrodes. The shallow peaks in the densities at $z = \pm 2.0$ nm show that particles can pass through the pore, though the valleys at both sides of these peaks indicate that crossing events are relatively rare. The passage of ions through these pores is also attested to by the accumulation of all anions (cations) on the right (left) electrode, while the simulations started with homogeneous distributions. The mirror-symmetry of the ion distributions, the agreement between GCPM and CPM in Table II and Fig. 7, and the time evolution of the charges on the electrodes (data not shown) all suggest that the simulations have converged to equilibrium. Sampling this equilibrium state proceeds too slowly, however, to extract a reliable value of the ion-related capacitance from the electrode charge fluctuations (see Table I). In the quantization of the agreement between CPM and GCPM, the null hypothesis is rejected for 10.7% of bins for the anions and for 0.5% of bins for the cations.

D. Ionic liquid between copper electrodes

The ion density distributions for $[BMIM^+][BF_4^-]$ in Fig. 8 are the result of a 5 ns equilibration run followed by a 10 ns production run, together requiring about 8 days on 36 cores using CPM. The distributions are not symmetric, despite the zero potential difference between the two identical electrodes. Inspection of movies of these simulations in visual molecular dynamics (VMD)[57] reveals that the molecules at the copper electrodes form a frozen layer in both CPM and GCPM. Switching to constant vanishing charges on the electrode atoms does not notably alter this behavior. Molecules further removed from the electrodes diffuse at about 2×10^{-7} cm^2/s, comparable to the bulk fluid. The freezing of ionic liquids at interfaces and under confinement has been reported by a number of groups.[58–62] Because of the immobile interfacial layer, which was also observed in simulations using ELECTRODE at elevated temperatures of 400 and 500 K, it is not meaningful to compare ensemble averaged simulation results from GCPM and CPM.

When the penalty in GCPM is turned off, $K' = 0$, the ion-induced charges on the electrode atoms grow to unrealistically high values, ranging up to $\pm 2 \times 10^3 e$ after 1 fs, requiring a time step of 0.01 fs. The charges adopt regular patterns, as illustrated in Fig. 9(a);
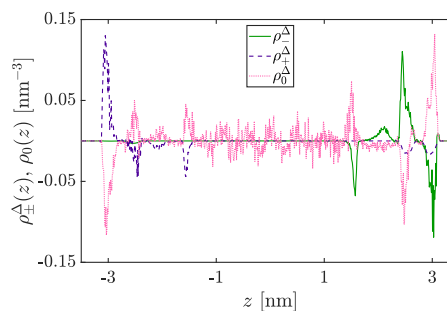

FIG. 6. Effect of the strength of the penalty in GCPM, for (a) $K' = 0$, (b) $K' = \sqrt{2/\pi}\,\eta = 1.579$ Å^{-1}, and (c) $K' = 10$ Å^{-1}, on the density profiles of cations (green), cations (blue), and solvent (pink) between two porous electrodes [see Fig. 1(c)]. The positions of the inner electrode layers are indicated with vertical dashed–dotted lines, and the positions of the outer electrode layers coincide with the boundaries of the plots.

FIG. 7. The differences between the density profiles of anions, cations, and solvent particles between model porous electrodes [see Fig. 1(c)] as obtained with GCPM and CPM at their default settings.
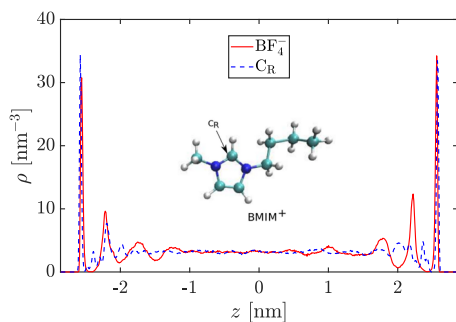
FIG. 8. Number densities of the carbon atom C_R of BMIM$^+$ and the boron atom of BF$_4^-$ for this room-temperature ionic liquid between copper electrodes at vanishing potential difference in CPM.
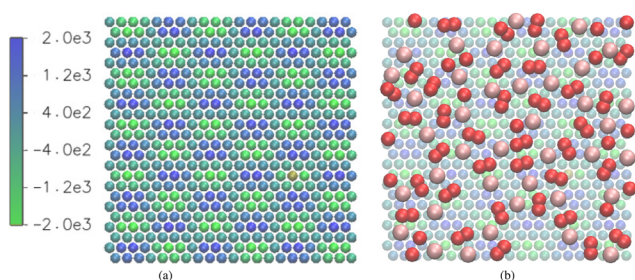

FIG. 9. Simulations of the ionic liquid [BMIM$^+$][BF$_4^-$] between copper electrodes highlight the importance of a penalty function restraining the charge fluctuations of the electrode atoms. (a) A regular pattern of excessive charges develops within a femtosecond of turning off the penalty in GCPM, $K' = 0$; the electrode atoms are colored by their charge, with the legend indicating charges in multiples of the elementary charge. (b) The ions at the interface remain disordered, suggesting they are not able to follow the rapidly growing charges; only the nitrogen atoms of BMIM$^+$ (red) and boron atoms of BF$_4^-$ (pink) are shown.

the ions in the layer adjacent to the wall do not show the same pattern, see Fig. 9(b), probably due to the short time scale and their slow dynamics. The charges continue to grow, enabling the correspondingly increased Coulomb forces to pull ions into the electrode layer in defiance of the Lennard-Jones interactions and causing the simulation to crash after about 2 fs. Using the default value of $K' = 1.579$ Å^{-1}, or CPM with the default value $\eta = 1.979$ Å^{-1}, already suffices to limit the atomic charge fluctuations to a bandwidth of about $0.05e$ around an average value close to zero.

E. Algorithm complexity

The algorithmic complexity of simulations using CPM,[25] GCPM, and ELECTRODE[32] is tested for the above four example systems. Simulation boxes are enlarging through repeated doubling of the extensive system dimensions, alternating between (nearly) square and rectangular electrode areas. The run times of these systems increase linearly with the number of simulation steps (data not shown). Run times per step, t_{step}, are shown in Fig. 10 on a double logarithmic scale, using two horizontal axes to facilitate comparison with the anticipated scaling laws. The straight lines fit Eq. (29), yielding the fit parameters collected in Table III. Assuming that the

electrostatic calculation dominates the time complexity, we expect a power law for the CPM simulations with a power b between 1.5 and 2.0.[22,23] The fitted powers, bold-faced in Table III, all lie in this range. The two highest scaling powers are observed for the two systems
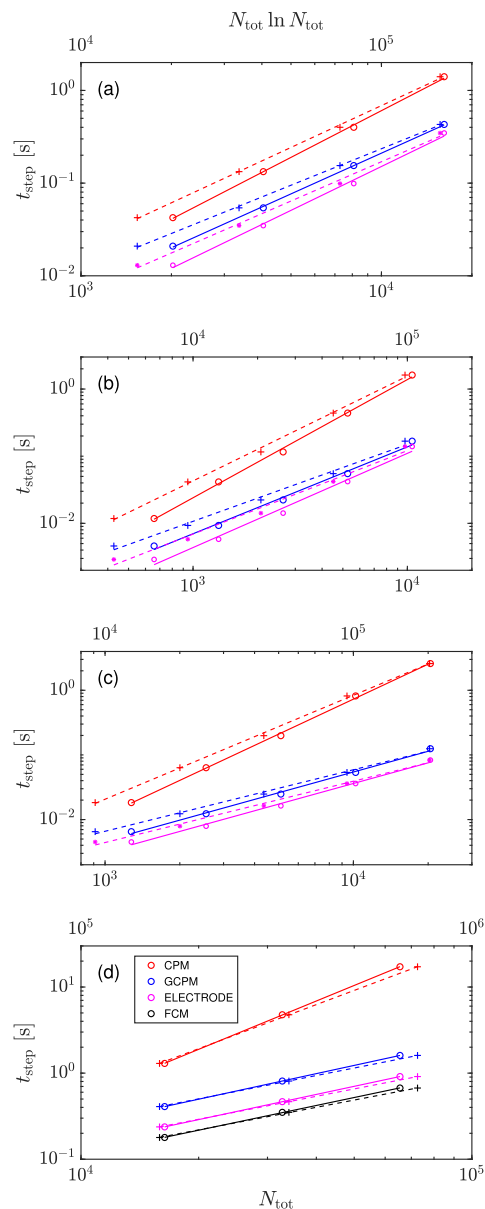

FIG. 10. CPU time per time step as functions of the number of particles in the simulation box, N_{tot}, for (a) an ionic solution between graphene-like electrodes, (b) an ionic solution between FCC electrodes, (c) an ionic solution between porous electrodes, and (d) the ionic liquid [BMIM$^+$][BF$_4^-$] between copper electrodes. Solid lines and circular markers relate to the bottom N_{tot} axis, while dashed lines and pluses relate to the top N_{tot} ln N_{tot} axis. The lines are fits using the scaling laws of Eq. (29), with fit parameters collected in Table III. The charges of the electrode atoms are calculated by Ewald summation (CPM), via PPPM (GCPM and ELECTRODE), or kept fixed (FCM).

TABLE III. Fit parameters for the CPU time per simulation time step t_{step}, as presented for four systems in Fig. 10, using the scaling laws of Eq. (29) with N_{tot} the total number of atoms in the system. The charges of the electrode atoms are calculated by Ewald summation (CPM), by standard PPPM (GCPM), by an adapted PPPM routine (ELECTRODE), or kept fixed (FCM). The key values in this table are bold-faced.

System	Method	$a\ [10^{-6}\ s]$	$b\ [-]$	$c\ [10^{-7}\ s]$	$d\ [-]$
Graphene $\Delta V = 0.2$ V	CPM	0.12	**1.67**	0.22	1.50
	GCPM	0.30	1.46	0.68	**1.31**
	ELECTRODE	0.078	1.57	0.15	**1.41**
FCC $\Delta V = 0.2$ V	CPM	0.13	**1.76**	0.25	1.56
	GCPM	0.92	1.29	2.8	**1.15**
	ELECTRODE	0.27	1.40	0.74	**1.24**
Porous $\Delta V = 2$ V	CPM	0.047	**1.80**	0.076	1.61
	GCPM	3.0	1.06	10	**0.95**
	ELECTRODE	2.1	1.06	7.1	**0.95**
Ionic liquid $\Delta V = 0$ V	CPM	0.018	**1.87**	0.018	1.70
	GCPM	28	0.99	85	**0.90**
	ELECTRODE	19	0.97	59	**0.89**
	FCM	17	0.95	53	**0.87**

with the highest number density of electrolyte particles. In simulations using GCPM and ELECTRODE, we expect the run times to follow PPPM's scaling law, $\mathcal{O}(N_{tot} \ln N_{tot})$. Fits with a power-law variation on this scaling law [see Eq. (29b)] are included in Fig. 10. Three out of four fitted powers d, bold-faced in Table III, are sufficiently close to the theoretical value of $d = 1$ to support the conclusion that GCPM scales as expected; the one exception is the system with graphene electrodes, possibly because the high number density of atoms in the electrodes and the low number density of ions in the electrolyte tip the balance between real space and reciprocal space calculations in PPPM toward the former. For the two dilute systems, see Figs. 1(a) and 1(b), the fitted powers d obtained with ELECTRODE are higher by about 0.1 than their counterparts with GCPM, while ELECTRODE realizes prefactors c amounting to about 25% of their GCPM counterparts. Hence, GCPM may be faster than ELECTRODE for very large systems in these cases. For the two dense systems, see Figs. 1(c) and 1(d), ELECTRODE yields powers d nearly identical to those for GCPM, while the prefactors are about 30% lower than those for GCPM. Hence, GCPM scales the same as ELECTRODE, but its current naïve implementation requires around 75% more CPU time per step.

Curiously, the system with graphene electrodes shows both the worst scaling behavior in the PPPM-based approaches and the best scaling behavior in the Ewald summation (see Table III). Figure 10(a) shows, however, that GCPM is still nearly twice as fast as CPM for the smallest system size explored here, and this ratio grows modestly with increasing system size. Conversely, PPPM-based approaches show their best scaling behavior, and Ewald summation its worst, for the all-atom ionic liquid system. GCPM is just over three times faster than CPM at the smallest system size, growing to more than ten times faster by a fourfold increase in N_{tot} [see Fig. 10(d)]. For this system, we also present simulations with the fixed charge method (FCM), mimicking a vanishing

potential difference by setting all electrode charges to zero. Figure 10(d) and Table III show that FCM simulations—using PPPM for the electrostatic interactions—and GCPM simulations share essentially identical time complexities. The CPU time per step for GCPM equates to ~ 2.3 steps with FCM. These observations indicate that our naive implementation of GCPM approaches the best performance realizable with an off-the-shelf implementation of PPPM, with the doubling of t_{step} between FCM and GCPM largely explained by the one additional invocation of PPPM in every GCPM step to calculate the Coulombic energies of all electrode atoms. It is evident that GCPM's use of a standard PPPM routine to obtain the potentials on all electrode atoms incurs several superfluous calculations: this invocation of PPPM with the test charges $\boldsymbol{Q}' = Q'\boldsymbol{D}$ also computes energies and forces on all electrolyte atoms, as well as forces on all electrode atoms. A dedicated electrostatic solver—or a generic solver with the ability to skip the aforementioned superfluous evaluations—would reduce the computational demands. The ELECTRODE routine, with its dedicated modifications of PPPM, reduces the CPU time per step to ~ 1.3 steps with FCM. The agreement on the power d across all three PPPM-based simulations indicates that the matrix-vector multiplications to solve the electrodes' atomic charges in GCPM and ELECTRODE do not noticeably raise their time complexity over that of FCM for the system sizes studied here.

V. CONCLUSION AND OUTLOOK

We presented a generalized approach to simulating conducting electrodes at a fixed potential difference, GCPM, which we implemented in LAMMPS[45] to work in conjunction with its existing PPPM routine. Simulation results on four sample systems show good agreement between GCPM and a traditional Ewald-based

CPM, while GCPM is computationally considerably cheaper, easier to implement, and more flexible.

We showed that the narrow Gaussian spreading of the charges on the electrode atoms, as traditionally employed in constant potential simulations, makes a negligible impact on the interatomic forces. Treating these atoms as point charges, like the atoms of the electrolyte, enables constant potential simulations by invocations of any existing efficient standard electrostatic routine. However, the use of narrow Gaussians does have an important impact on the electrostatic energy: it effectively endows each electrode atom with an internal energy quadratic in its charge. From a physical point of view, an energy penalty of this form offers an appealing route to account for the atom's restricted ability to gain or lose electrons. The same effect is, therefore, realized in GCPM by simply including an intra-atomic energy quadratic in the charges. A term linear in the energy can be added to account for chemical differences in electron affinities between unlike atoms or environment-induced differences between atoms at the surface vs atoms in the bulk. In the absence of a penalty restraining the charge fluctuations, the ions may induce unrealistic charging patterns on the electrodes with oscillations either perpendicular or parallel to the surface. A penalty with strength $K' \approx 1.6$ Å^{-1}, equivalent to the intra-atomic energies in CPM at the common Gaussian spreading parameter $\eta \approx 2.0$ Å^{-1}, suffices to suppress these spurious oscillations. More research is needed to establish accurate penalties for electrode materials.

As an example, we compare an existing CPM routine for LAMMPS, employing a dedicated Ewald routine for the narrow Gaussian spreading, with a GCPM implementation invoking the standard PPPM library. Simulations on four sample systems showed that CPM and GCPM produce equivalent results. The run times per step are in agreement with textbook scaling laws: $\mathcal{O}(N^{3/2})$ to $\mathcal{O}(N^2)$ for CPM based on Ewald summation and $\mathcal{O}(N \ln N)$ for GCPM based on PPPM, with N the total number of atoms in the system. The latter scaling law is also found for a recent CPM implementation in LAMMPS by Ahrens-Iwers and Meißner,[31] based on a dedicated PPPM routine re-coded to fit in with CPM. These PPPM-based methods enable constant potential simulations of more elaborate models over longer periods of time and thereby open up new possibilities to investigate the operations of supercapacitors. A future routine combining the features of GCPM, ELECTRODE, MetalWalls, and ICC* may result in an even faster and more realistic method for the simulation of induced fluctuating charges on electrodes.

ACKNOWLEDGMENTS

AUTHOR DECLARATIONS

Conflict of Interest

The authors have no conflicts to disclose.

Author Contributions

Ranisha S. Sitlapersad: Conceptualization (supporting); Data curation (lead); Formal analysis (lead); Investigation (lead); Methodology (supporting); Project administration (equal); Software (lead); Validation (lead); Visualization (lead); Writing – original draft (lead); Writing – review & editing (equal). **Anthony R. Thornton**: Conceptualization (lead); Funding acquisition (lead); Methodology (supporting); Project administration (equal); Resources (equal); Software (supporting); Supervision (equal); Writing – review & editing (equal). **Wouter K. den Otter**: Conceptualization (lead); Formal analysis (supporting); Methodology (lead); Project administration (equal); Resources (equal); Software (supporting); Supervision (equal); Validation (supporting); Visualization (supporting); Writing – original draft (supporting); Writing – review & editing (equal).

DATA AVAILABILITY

The data that support the findings of this study are available from the corresponding author upon reasonable request.

APPENDIX: THE ELECTROSTATIC ENERGY

Ewald summation allows the calculation of electrostatic energies and forces for neutral simulation boxes with periodic boundary conditions. All atoms are treated as point charges interacting through long-range Coulomb interactions. To facilitate the calculation of slowly converging sums over increasingly distant neighbors, atom-based Gaussian charge distributions of width α^{-1} are added and subtracted to split the problem into two summations—one in real space and one in reciprocal space—that both converge rapidly. Three-dimensional Ewald summation with slab correction[21–23,27,37] for a neutral simulation box containing N electrode atoms of charges Q_i at positions $\boldsymbol{R}_i$ and n electrolyte atoms of charges q_i at positions $\boldsymbol{r}_i$ gives the total electrostatic energy as

$$
\begin{aligned}
4\pi\varepsilon_0 U_e &= \frac{2\pi}{V}\sum_{\boldsymbol{k}\neq 0}\frac{1}{k^2}|S(\boldsymbol{k})|^2 e^{-k^2/(4\alpha^2)} + \frac{1}{2}\sum_{i=1}^{n}\sum_{\substack{j=1\\j\neq i}}^{n} q_i q_j \frac{\text{erfc}(\alpha|\boldsymbol{r}_i - \boldsymbol{r}_j|)}{|\boldsymbol{r}_i - \boldsymbol{r}_j|} \\
&+ \sum_{i=1}^{N}\sum_{j=1}^{n} Q_i q_j \frac{\text{erfc}(\alpha|\boldsymbol{R}_i - \boldsymbol{r}_j|)}{|\boldsymbol{R}_i - \boldsymbol{r}_j|} + \frac{1}{2}\sum_{i=1}^{N}\sum_{\substack{j=1\\j\neq i}}^{N} Q_i Q_j \frac{\text{erfc}(\alpha|\boldsymbol{R}_i - \boldsymbol{R}_j|)}{|\boldsymbol{R}_i - \boldsymbol{R}_j|} \\
&- \frac{\alpha}{\sqrt{\pi}}\left(\sum_{i=1}^{N} Q_i^2 + \sum_{i=1}^{n} q_i^2\right) + \frac{2\pi}{V}\left(\sum_{i=1}^{N} Q_i Z_i + \sum_{i=1}^{n} q_i z_i\right)^2,
\end{aligned}
\tag{A1}
$$

with dielectric permittivity of vacuum ε_0, volume of the box V, reciprocal lattice vectors $\boldsymbol{k}$ commensurate with the dimensions of the periodic box and length $k = |\boldsymbol{k}|$, the complementary error function erfc, the elevations Z_i and z_i of electrode and electrolyte atoms relative to the midplane of the slab, and charge-weighted structure factors

$$
S(\boldsymbol{k}) = \sum_{j=1}^{N} Q_j e^{i\boldsymbol{k}\cdot\boldsymbol{R}_j} + \sum_{j=1}^{n} q_j e^{i\boldsymbol{k}\cdot\boldsymbol{r}_j}.
\tag{A2}
$$

The elements of the matrix $\mathbf{A}$ in Eq. (3) are extracted from the above-mentioned expression as

$$4\pi\varepsilon_0 A_{ij} = \frac{4\pi}{V}\sum_{\mathbf{k}\neq 0}\frac{1}{k^2}\cos\left[\mathbf{k}\cdot(\mathbf{R}_i-\mathbf{R}_j)\right]e^{-k^2/(4\alpha^2)}$$
$$+ \frac{\mathrm{erfc}(\alpha|\mathbf{R}_i-\mathbf{R}_j|)}{|\mathbf{R}_i-\mathbf{R}_j|}(1-\delta_{ij}) - \frac{\alpha}{\sqrt{\pi}}\delta_{ij} + \frac{2\pi}{V}Z_iZ_j, \quad (A3)$$

with δ_{ij} the Kronecker delta. Note that the diagonal elements A_{ii} are all identical, save for their quadratic dependence on the elevation Z_i.

In traditional CPM, the charges of the electrode atoms are treated as narrow Gaussians of width η^{-1} and total charge Q_i,

$$\bar{Q}_i(\mathbf{x}) = Q_i\left(\frac{\eta^2}{\pi}\right)^{3/2}e^{-\eta^2(\mathbf{x}-\mathbf{R}_i)^2}, \quad (A4)$$

rather than point charges, resulting in the energy[12,25,37]

$$4\pi\varepsilon_0 U_e^{\mathrm{CPM}} = \frac{2\pi}{V}\sum_{\mathbf{k}\neq 0}\frac{1}{k^2}|S(\mathbf{k})|^2 e^{-k^2/(4\alpha^2)} + \frac{1}{2}\sum_{i=1}^{n}\sum_{\substack{j=1\\j\neq i}}^{n}q_iq_j\frac{\mathrm{erfc}(\alpha|\mathbf{r}_i-\mathbf{r}_j|)}{|\mathbf{r}_i-\mathbf{r}_j|}$$
$$+ \sum_{i=1}^{N}\sum_{j=1}^{n}Q_iq_j\frac{\mathrm{erfc}(\alpha|\mathbf{R}_i-\mathbf{r}_j|)-\mathrm{erfc}(\eta|\mathbf{R}_i-\mathbf{r}_j|)}{|\mathbf{R}_i-\mathbf{r}_j|}$$
$$+ \frac{1}{2}\sum_{i=1}^{N}\sum_{\substack{j=1\\j\neq i}}^{N}Q_iQ_j\frac{\mathrm{erfc}(\alpha|\mathbf{R}_i-\mathbf{R}_j|)-\mathrm{erfc}\left(\frac{\eta|\mathbf{R}_i-\mathbf{R}_j|}{\sqrt{2}}\right)}{|\mathbf{R}_i-\mathbf{R}_j|}$$
$$+ \left(\underline{\frac{\eta}{\sqrt{2\pi}}} - \frac{\alpha}{\sqrt{\pi}}\right)\sum_{i=1}^{N}Q_i^2 - \frac{\alpha}{\sqrt{\pi}}\sum_{i=1}^{n}q_i^2$$
$$+ \frac{2\pi}{V}\left(\sum_{i=1}^{N}Q_iZ_i + \sum_{i=1}^{n}q_iz_i\right)^2. \quad (A5)$$

The importance of the underlined contribution is discussed in the main text [see Eq. (5)].

REFERENCES

[1]E. Hossain, H. M. R. Faruque, M. S. H. Sunny, N. Mohammad, and N. Nawar, "A comprehensive review on energy storage systems: Types, comparison, current scenario, applications, barriers, and potential solutions, policies, and future prospects," Energies **13**, 3651 (2020).

[2]A. González, E. Goikolea, J. A. Barrena, and R. Mysyk, "Review on supercapacitors: Technologies and materials," Renewable Sustainable Energy Rev. **58**, 1189–1206 (2016).

[3]K. PoonamSharma, K. Sharma, A. Arora, and S. Tripathi, "Review of supercapacitors: Materials and devices," J. Energy Storage **21**, 801–825 (2019).

[4]C. Merlet, B. Rotenberg, P. A. Madden, P.-L. Taberna, P. Simon, Y. Gogotsi, and M. Salanne, "On the molecular origin of supercapacitance in nanoporous carbon electrodes," Nat. Mater. **11**, 306–310 (2012).

[5]C. Péan, C. Merlet, B. Rotenberg, P. A. Madden, P.-L. Taberna, B. Daffos, M. Salanne, and P. Simon, "On the dynamics of charging in nanoporous carbon-based supercapacitors," ACS Nano **8**, 1576–1583 (2014).

[6]K. Breitsprecher, M. Abele, S. Kondrat, and C. Holm, "The effect of finite pore length on ion structure and charging," J. Chem. Phys. **147**, 104708 (2017).

[7]K. Breitsprecher, C. Holm, and S. Kondrat, "Charge me slowly, I am in a hurry: Optimizing charge–discharge cycles in nanoporous supercapacitors," ACS Nano **12**, 9733–9741 (2018).

[8]T. Mendez-Morales, M. Burbano, M. Haefele, B. Rotenberg, and M. Salanne, "Ion-ion correlations across and between electrified graphene layers," J. Chem. Phys. **148**, 193812 (2018).

[9]T. Méndez-Morales, N. Ganfoud, Z. Li, M. Haefele, B. Rotenberg, and M. Salanne, "Performance of microporous carbon electrodes for supercapacitors: Comparing graphene with disordered materials," Energy Storage Mater. **17**, 88–92 (2019).

[10]E. H. Lahrar, A. Belhboub, P. Simon, and C. Merlet, "Ionic liquids under confinement: From systematic variations of the ion and pore sizes toward an understanding of the structure and dynamics in complex porous carbons," ACS Appl. Mater. Interfaces **12**, 1789–1798 (2020).

[11]E. H. Lahrar, I. Deroche, C. Matei Ghimbeu, P. Simon, and C. Merlet, "Simulations of ionic liquids confined in surface-functionalized nanoporous carbons: Implications for energy storage," ACS Appl. Nano Mater. **4**, 4007–4015 (2021).

[12]J. I. Siepmann and M. Sprik, "Influence of surface topology and electrostatic potential on water/electrode systems," J. Chem. Phys. **102**, 511–524 (1995).

[13]S. K. Reed, O. J. Lanning, and P. A. Madden, "Electrochemical interface between an ionic liquid and a model metallic electrode," J. Chem. Phys. **126**, 084704 (2007).

[14]H. Nakano and H. Sato, "A chemical potential equalization approach to constant potential polarizable electrodes for electrochemical-cell simulations," J. Chem. Phys. **151**, 164123 (2019).

[15]S. Tyagi, M. Süzen, M. Sega, M. Barbosa, S. S. Kantorovich, and C. Holm, "An iterative, fast, linear-scaling method for computing induced charges on arbitrary dielectric boundaries," J. Chem. Phys. **132**, 154112 (2010).

[16]A. Arnold, K. Breitsprecher, F. Fahrenberger, S. Kesselheim, O. Lenz, and C. Holm, "Efficient algorithms for electrostatic interactions including dielectric contrasts," Entropy **15**, 4569–4588 (2013).

[17]I. L. Geada, H. Ramezani-Dakhel, T. Jamil, M. Sulpizi, and H. Heinz, Nat. Commun. **9**, 716 (2018).

[18]L. Scalfi, M. Salanne, and B. Rotenberg, Annu. Rev. Phys. Chem. **72**, 189–212 (2021).

[19]G. Jeanmairet, B. Rotenberg, and M. Salanne, "Microscopic simulations of electrochemical double-layer capacitors," Chem. Rev. **122**, 10860–10898 (2022).

[20]S. Kondrat, G. Feng, F. Bresme, M. Urbakh, and A. A. Kornyshev, "Theory and simulations of ionic liquids in nanoconfinement," Chem. Rev. **123**, 6668–6715 (2023).

[21]C. Kittel, *Introduction to Solid State Physics*, 6th ed. (John Wiley & Sons, Inc., New York, 1986).

[22]D. Frenkel and B. Smit, *Understanding Molecular Simulations. From Algorithms to Applications*, 2nd ed. (Academic Press, San Diego, CA, 2002).

[23]M. P. Allen and D. J. Tildesley, *Computer Simulation of Liquids*, 2nd ed. (Oxford University Press, Oxford, 2017).

[24]D. T. Limmer, C. Merlet, M. Salanne, D. Chandler, P. A. Madden, R. van Roij, and B. Rotenberg, "Charge fluctuations in nanoscale capacitors," Phys. Rev. Lett. **111**, 106102 (2013).

[25]Z. Wang, Y. Yang, D. L. Olmsted, M. Asta, and B. B. Laird, "Evaluation of the constant potential method in simulating electric double-layer capacitors," J. Chem. Phys. **141**, 184102 (2014).

[26]A. Coretti, C. Bacon, R. Berthin, A. Serva, L. Scalfi, I. Chubak, K. Goloviznina, M. Haefele, A. Marin-Laflèche, B. Rotenberg, S. Bonella, and M. Salanne, "MetalWalls: Simulating electrochemical interfaces between polarizable electrolytes and metallic electrodes," J. Chem. Phys. **157**, 184801 (2022).

[27]I.-C. Yeh and M. L. Berkowitz, "Ewald summation for systems with slab geometry," J. Chem. Phys. **111**, 3155–3162 (1999).

[28]T. R. Gingrich and M. Wilson, "On the ewald summation of Gaussian charges for the simulation of metallic surfaces," Chem. Phys. Lett. **500**, 178–183 (2010).

[29]S. R. Tee and D. J. Searles, "Fully periodic, computationally efficient constant potential molecular dynamics simulations of ionic liquid supercapacitors," J. Chem. Phys. **156**, 184101 (2022).

[30]R. W. Hockney and J. W. Eastwood, *Computer Simulation Using Particles* (Adam Hilger, Bristol, U.K., 1989).

[31]L. J. V. Ahrens-Iwers and R. H. Meißner, "Constant potential simulations on a mesh," J. Chem. Phys. **155**, 104104 (2021).

[32]L. J. V. Ahrens-Iwers, M. Janssen, S. R. Tee, and R. H. Meißner, "ELECTRODE: An electrochemistry package for atomistic simulations," J. Chem. Phys. 157, 084801 (2022).

[33]L. Scalfi, T. Dufils, K. G. Reeves, B. Rotenberg, and M. Salanne, "A semiclassical Thomas–Fermi model to tune the metallicity of electrodes in molecular simulations," J. Chem. Phys. 153, 174704 (2020).

[34]S. Plimpton, "Fast parallel algorithms for short-range molecular dynamics," J. Comput. Phys. 117, 1–19 (1995).

[35]See https://www.lammps.org/ for Lammps molecular dynamics simulator, 2024.

[36]A. Y. Toukmaji and J. A. Board, Jr., "Ewald summation techniques in perspective: A survey," Comput. Phys. Commun. 95, 73–92 (1996).

[37]T. Gingrich, "Simulating surface charge effects in carbon nanotube templated ionic crystal growth," Master's thesis, University of Oxford, England, 2010.

[38]M. Buraschi, S. Sansotta, and D. Zahn, "Polarization effects in dynamic interfaces of platinum electrodes and ionic liquid phases: A molecular dynamics study," J. Phys. Chem. C 124, 2002–2007 (2020).

[39]A. K. Rappe and W. A. Goddard III, "Charge equilibration for molecular dynamics simulations," J. Phys. Chem. 95, 3358–3363 (1991).

[40]See https://en.wikipedia.org/wiki/Ionization_energies_of_the_elements_(data_page) for more information about Ionization Energies of the Elements; accessed 28 June 2023.

[41]See https://en.wikipedia.org/wiki/Work_function for more information about Work function; accessed 28 June 2023.

[42]O. Leenaerts, B. Partoens, F. M. Peeters, A. Volodin, and C. Van Haesendonck, "The work function of few-layer graphene," J. Phys. Condens. Matter 29, 035003 (2016).

[43]L. Scalfi, D. T. Limmer, A. Coretti, S. Bonella, P. A. Madden, M. Salanne, and B. Rotenberg, "Charge fluctuations from molecular simulations in the constant-potential ensemble," Phys. Chem. Chem. Phys. 22, 10480–10489 (2020).

[44]J. B. Haskins and J. W. Lawson, "Evaluation of molecular dynamics simulation methods for ionic liquid electric double layers," J. Chem. Phys. 144, 184707 (2016).

[45]A. P. Thompson, H. M. Aktulga, R. Berger, D. S. Bolintineanu, W. M. Brown, P. S. Crozier, P. J. in't Veld, A. Kohlmeyer, S. G. Moore, T. D. Nguyen, R. Shan, M. J. Stevens, J. Tranchida, C. Trott, S. J. Plimpton, and S. J. Plimpton, "LAMMPS—A flexible simulation tool for particle-based materials modeling at the atomic, meso, and continuum scales," Comput. Phys. Commun. 271, 108171 (2022).

[46]Z. Wang, Y. Yang, D. L. Olmsted, M. Asta, and B. B. Laird, https://github.com/zhenxingwang/lammps-conp, 2014.

[47]R. S. Sitlapersad, A. R. Thornton, and W. K. den Otter, https://github.com/r-s-sitlapersad/lammps, 2023.

[48]P. Cats, R. S. Sitlapersad, W. K. den Otter, A. R. Thornton, and R. van Roij, "Capacitance and structure of electric double layers: Comparing Brownian dynamics and classical density functional theory," J. Solution Chem. 51, 296–319 (2022).

[49]J. N. Canongia Lopes, J. Deschamps, and A. A. H. Pádua, "Modeling ionic liquids using a systematic all-atom force field," J. Phys. Chem. B 108, 2038–2047 (2004); 108, 11250 (2004).

[50]J. N. Canongia Lopes and A. A. H. Pádua, "Molecular force field for ionic liquids III: Imidazolium, pyridinium, and phosphonium cations; chloride, bromide, and dicyanamide anions," J. Phys. Chem. B 110, 19586–19592 (2006).

[51]A. Mondal and S. Balasubramanian, "Quantitative prediction of physical properties of imidazolium based room temperature ionic liquids through determination of condensed phase site charges: A refined force field," J. Phys. Chem. B 118, 3409–3422 (2014).

[52]J.-P. Ryckaert, G. Ciccotti, and H. J. Berendsen, "Numerical integration of the cartesian equations of motion of a system with constraints: Molecular dynamics of n-alkanes," J. Comput. Phys. 23, 327–341 (1977).

[53]V. P. Filippova, S. A. Kunavin, and M. S. Pugachev, "Calculation of the parameters of the Lennard-Jones potential for pairs of identical atoms based on the properties of solid substances," Inorg. Mater. Appl. Res. 6, 1–4 (2015).

[54]MATLAB version: 9.13.0 (R2022b), The MathWorks Inc., Natick, MA, USA.

[55]Z. Li, G. Jeanmairet, T. Méndez-Morales, B. Rotenberg, and M. Salanne, "Capacitive performance of water-in-salt electrolytes in supercapacitors: A simulation study," J. Phys. Chem. C 122, 23917–23924 (2018).

[56]A. Serva, L. Scalfi, B. Rotenberg, and M. Salanne, "Effect of the metallicity on the capacitance of gold–aqueous sodium chloride interfaces," J. Chem. Phys. 155, 044703 (2021).

[57]W. Humphrey, A. Dalke, and K. Schulten, "VMD: Visual molecular dynamics," J. Mol. Graph. 14, 33–38 (1996).

[58]M. Drüschler, N. Borisenko, J. Wallauer, C. Winter, B. Huber, F. Endres, and B. Roling, "New insights into the interface between a single-crystalline metal electrode and an extremely pure ionic liquid: Slow interfacial processes and the influence of temperature on interfacial dynamics," Phys. Chem. Chem. Phys. 14, 5090–5099 (2012).

[59]B. Rotenberg and M. Salanne, "Structural transitions at ionic liquid interfaces," J. Phys. Chem. Lett. 6, 4978–4985 (2015).

[60]J. Comtet, A. Niguès, V. Kaiser, B. Coasne, L. Bocquet, and A. Siria, "Nanoscale capillary freezing of ionic liquids confined between metallic interfaces and the role of electronic screening," Nat. Mater. 16, 634–639 (2017).

[61]M. Busch, T. Hofmann, B. Frick, J. P. Embs, B. Dyatkin, and P. Huber, "Ionic liquid dynamics in nanoporous carbon: A pore-size- and temperature-dependent neutron spectroscopy study on supercapacitor materials," Phys. Rev. Mater. 4, 055401 (2020).

[62]N. C. Osti and E. Mamontov, "Microscopic dynamics in room-temperature ionic liquids confined in materials for supercapacitor applications," Sustainable Energy Fuels 4, 1554–1576 (2020).